

PAPER

An edge-on charge-transfer design for energy-resolved x-ray detection

To cite this article: Zaifeng Shi *et al* 2016 *Phys. Med. Biol.* **61** 4183

View the [article online](#) for updates and enhancements.

Related content

- [Energy-resolved CT imaging with a photon-counting silicon-strip detector](#)
Mats Persson, Ben Huber, Staffan Karlsson *et al.*
- [Spectral CT imaging of vulnerable plaque with two independent biomarkers](#)
Pavlo Baturin, Yahya Alivov and Sabee Molloi
- [Photon-counting spectral computed tomography using silicon strip detectors](#)
Hans Bornefalk and Mats Danielsson

Recent citations

- [Yikai Su *et al*](#)



The advertisement features the Quasar MRID3D logo on the left, which includes a stylized 'Q' with a crosshair. The text reads: 'The Best Way to QUANTIFY MRI GEOMETRIC DISTORTION IN 3D!'. In the center is a photograph of the MRID3D device, a cylindrical metal frame with blue straps and internal components. On the right is the ModusRA logo, a green square with a stylized 'Q' and the text 'modusRA' and 'Accuracy. Confidence.™' below it.

An edge-on charge-transfer design for energy-resolved x-ray detection

Zaifeng Shi¹, Haoyu Yang¹, Wenxiang Cong² and Ge Wang²

¹ School of Electronic Information Engineering, Tianjin University, Tianjin, People's Republic of China

² Biomedical Imaging Center, Center for Biotechnology & Interdisciplinary Studies at Rensselaer, Department of Biomedical Engineering, Rensselaer Polytechnic Institute, Troy, New York, USA

E-mail: shizaifeng@tju.edu.cn and wangg6@rpi.edu

Received 31 December 2015, revised 13 March 2016

Accepted for publication 31 March 2016

Published 18 May 2016



Abstract

As an x-ray beam goes through the human body, it will collect important information via interaction with tissues. Since this interaction is energy-sensitive, the state-of-the-art spectral CT technologies provide higher quality images of biological tissues with x-ray energy information (or spectral information). With existing energy-integrating technologies, a large fraction of energy information is ignored in the x-ray detection process. Although the recently proposed photon-counting technology promises to achieve higher image quality at a lower radiation dose, it suffers from limitations in counting rate, performance uniformity, and fabrication cost. In this paper, we focus on an alternative approach to resolve the energy distribution of transmitted x-ray photons. First, we analyze the x-ray attenuation in a silicon substrate and describe a linear approximation model for x-ray detection. Then, we design an edge-on architecture based on the proposed energy-resolving model. In our design, the x-ray-photon-induced charges are transferred sequentially resembling the working process of a CCD camera. Finally, we numerically evaluate the linear approximation of x-ray attenuation and derive the energy distribution of x-ray photons. Our simulation results show that the proposed energy-sensing approach is feasible and has the potential to complement the photon-counting technology.

Keywords: computed tomography, x-ray detector, CCD, edge-on, energy-sensing

(Some figures may appear in colour only in the online journal)

1. Introduction

Spectral computed tomography (CT) is an emerging approach that can be used to obtain more tissue information in terms of energy-dependent x-ray linear attenuation coefficients.

X-ray detectors are the pivotal component of spectral CT. The current development of x-ray detectors aims to resolve the energy distribution of transmitted photons, i.e. their spectrum. There are two approaches that can be used to transform x-ray energy information into charge signals, direct conversion and indirect conversion (Doran *et al* 2001, Overdick *et al* 2009). Unlike the indirect conversion approach, which needs an intermediate step to convert x-ray radiation into light in a scintillating medium, the direct conversion approach converts x-ray energy into electrical charges. Photon counting is currently the most prevailing research area of direct conversion, which counts individual photons in an energy-discriminative fashion. Attenuation coefficients of x-ray photons rise rapidly when their energy levels are above the binding energy of *K*-shell electrons of atoms, and spectral CT with photon-counting detectors takes advantage of energy-sensitive properties in general and *K*-edge contrasts in particular, providing richer information of soft tissue (Pan *et al* 2010).

Energy-integrating and photon-counting detectors (PCD) are the two main solutions for conventional and spectral CT, respectively (Chu *et al* 2013). In the energy-integrating mode, the charge response due to radiation is analyzed in terms of total energy regardless of the energy distribution, and then a weighted average attenuation efficient at each pixel (or voxel) is derived to form the pixel value (Alvarez and Macovski 1976). In fact, the attenuation of x-rays varies as a function of x-ray energy, thus energy-dependent information is lost in conventional CT with energy-integrating detectors. On the other hand, photon-counting detectors resolve the energy distribution of x-ray photons, and were recently proven to be feasible with a silicon strip detector (Bornefalk and Danielsson 2010). In the photon-counting mode, the detector theoretically obtains both counts and their spectral information, and is capable of imaging various kinds of tissues if energy thresholds are properly set (Taguchi and Iwanczyk 2013). Furthermore, if appropriate material and readout device are used, the photon-counting scheme can provide a higher signal-to-noise ratio (SNR) than the traditional energy-integrating scheme (Shikhaliev 2009). To some extent, photon counting is able to obtain more information by detecting low energy components of x-ray (Giersch *et al* 2004). However, there is a main drawback with photon counting that high-speed control is required to tell whether an impulse is generated by one photon with high energy or several photons with lower energies (otherwise, leading to a pile-up effect) (Shikhaliev 2008, Taguchi *et al* 2010).

Cadmium telluride (CdTe) and cadmium zinc telluride (CTZ) are promising candidates for energy-resolving detectors (Shikhaliev 2008, Persson *et al* 2014), which have a high *z* number and a high attenuation efficiency for diagnostic x-rays. However, it takes time for CdTe/CTZ materials to collect and transfer charge responses since these materials have a relatively low charge mobility, therefore CdTe and CTZ detectors could suffer from the pile-up problem. Also, CdTe/CTZ has a higher manufacturing cost than silicon materials which have excellent electron mobility. Nevertheless, silicon has a low atomic number, thus x-ray detection sensors ought to be relatively thick (Persson *et al* 2014).

As far as the interaction between x-ray photons and atoms in a low atomic number material is concerned, photoelectric absorption and Compton scattering are the two main mechanisms. In the photoelectric effect, an x-ray photon is annihilated along with the generation of an electron. In this case, the generated charge density represents the photon density. Since photon absorption is depth and energy dependent, we can obtain the photon energy distribution from the generated charge density at different positions. However, since silicon has a relatively low atomic number, Compton scattering is more likely to happen when an x-ray beam of over 40 keV travels through a silicon layer. In the Compton effect, an x-ray photon usually generates several electrons, hence distorting the energy linearity of recorded data.

For charge information to be read out, the charge coupling approach can be applied. The silicon fabrication technology and CCD structure are mature, and can be adapted for x-ray detection. With a typical CCD camera for visible light detection, light signals are accepted from its gate side or substrate side, and transferred from the light to charge signals and read out by the corresponding readout circuit. However, when x-rays travel through a conventional silicon-based CCD, only a small fraction of the incident x-rays, which are at a relatively low energy, can be absorbed by the silicon. Although it is practical to use CCD to detect soft x-rays (Burke *et al* 1994), it is impractical for a general CCD camera to handle high energy x-rays which can travel in silicon material over centimeters before being fully absorbed. Therefore, an edge-on structure is a preferable solution to detect x-rays with a wide energy distribution (Lundqvist *et al* 1999).

Here we propose an energy-resolving model for spectral CT and its corresponding edge-on structure. In our design, x-rays enter the silicon bulk from one side, interact with atoms and generate electrons which can be collected in potential wells. Then, the collected charges can be consecutively transferred along the incident direction to the readout circuit for digitation.

The rest of this paper is organized as follows: section 2 describes our proposed x-ray detection model, edge-on structure and reconfigurable energy resolving method. Section 3 summarizes simulation results and demonstrates the feasibility of our approach. Section 4 discusses relevant issues and concludes the paper.

2. X-ray detection model

2.1. Photon absorption

While radiation can be absorbed in various materials, in this paper we focus on semiconductor materials especially silicon. When x-rays travel inside a silicon bulk, photons will interact with atoms and generate electrons. Absorbed photons in semiconductor materials can be formulated as,

$$G = \eta_0 \frac{P\lambda}{hc} \alpha e^{-\alpha y} \quad (1)$$

where η_0 is the internal quantum efficiency which indicates the amount of carrier pairs generated per photon, P is the x-ray intensity factor reflecting a cumulative effect of reflection, transmission and absorption along a ray path, λ is the wavelength of x-rays, h is Planck's constant, c is speed of light, and α is the mass attenuation coefficient related to wavelength and the imaginary part of the optical refraction index, and y is a relative distance into the material. The mass attenuation coefficient varies with photon energy; for more details, see the National Institute of Standards and Technology website.

Generally, medical x-rays have an energy range from 0.01 MeV to 0.14 MeV. The photoelectric effect describes the interaction between a photon and a bound orbital electron of an atom. Electrons within semiconductor material absorb the energy of incident photons. If the x-ray energy is greater than the band gap of the semiconductor, an electron is able to jump to the conduction band and becomes a free electron. Note that in this effect, the generation of charges follows an 'all or nothing' principle that one photon is annihilated and its energy is used to generate one electron and its kinetic energy. In Compton scattering, a large fraction of high energy photons are scattered in silicon, yielding a great uncertainty. Therefore, a more accurate model of photon-atom interaction is necessary.

For simplicity, equation (1) can be reduced to the following form (Gruner *et al* 2002):

$$\begin{cases} R = 0.090\rho^{-0.8}E^{1.3} & \text{for } E < 10 \text{ keV} \\ R = 0.045\rho^{-0.9}E^{1.7} & \text{for } E > 10 \text{ keV} \end{cases} \quad (2)$$

where E represents the incident beam energy, R is the thickness needed to thoroughly absorb the incident beam of the energy E , and ρ is the material density (Gruner *et al* 2002). This equation provides the solution to resolve the incident beam spectrum. For a silicon substrate particularly, the Fano factor is quite small (Bertolini and Coche 1968), which indicates that most of the intercepted energy contributes to the charge generation. Thus, the generated charge density can be represented by equation (3):

$$N \approx \frac{E}{E_0} \quad (3)$$

where E is the x-ray energy, and E_0 is the energy needed to generate one electron which is usually related to the material band gap. Equation (3) also indicates that the generated electron density is proportional to the photon energy/frequency. Hence, we can utilize the linearity to resolve the incident spectrum.

2.2. Energy-resolving methodology

Photon attenuation is related to material, thickness, and frequency. Usually, x-rays used in CT contain various energy levels ranging from 20 keV to 120 keV, and x-ray attenuation in a semiconductor material, such as silicon, takes the following process. When x-ray photons travel through a silicon material of a fixed thickness, photons will be absorbed at different levels to various degrees depending on the photon energy. At the same time, electrons are generated due to the absorption of photons. This procedure can be approximated in the following equation:

$$m_1E_1N_1a_{k1} + m_2E_2N_2a_{k2} + \dots + m_nE_nN_na_{kn} = g_k(x) \quad (4)$$

where E_i denotes a photon energy, N_i is the photon density at energy E_i , a_{ki} is the attenuation coefficient of photons with energy E_i for the given material thickness, m_i is an empirical coefficient which represents the number of generated charges by photons of energy E_i per energy unit, and $g_k(x)$ is the generated charge density within the silicon bulk with a specific thickness. Note that equation (4) is consistent with the linear approximation (equation (3) presented in subsection 2.1), and the assumption that the x-ray beam can be viewed as a linear combination of monochromatic radiations. On this occasion, to find the energy distribution, we just need to obtain N_i in equation (4). The more equations we have, the more accurately the energy spectrum will be resolved. That is, if we apply the same x-ray source on the same material and obtain charge information within different thicknesses (or layers), theoretically we can obtain as many as possible energy components. Note that E_i , a_{ki} and m_i can be obtained easily if the material and its thickness are defined, and the only issue is how to derive the amounts of generated charges through different layers.

There is a major advantage of this energy resolving method. While the required thickness to fully absorb an x-ray beam is determined by the radiation beam quality, we can adaptively change the layer thickness in the post-processing stage to maximize the spectral precision and minimize the system error. The details will be presented in the next subsection.

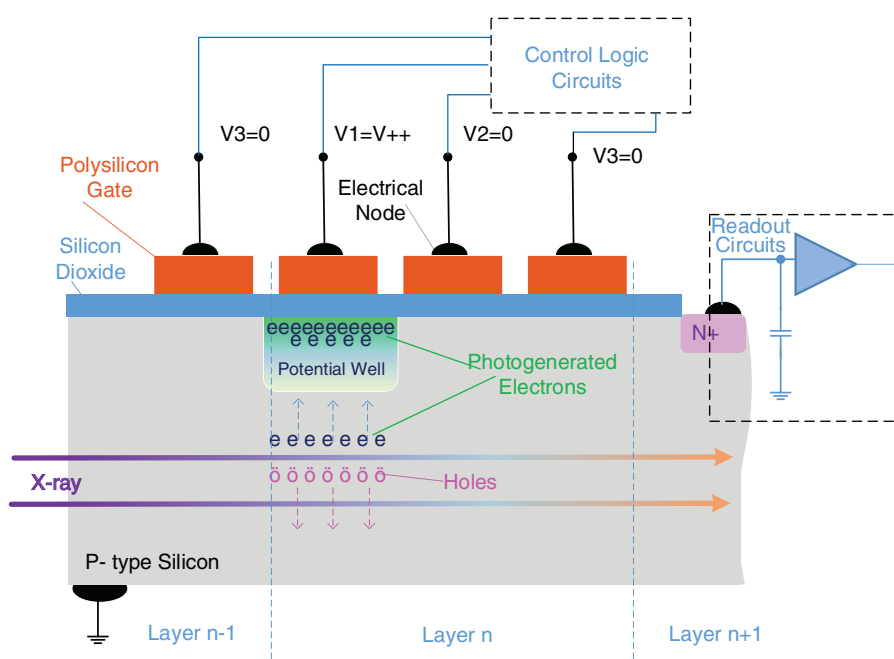


Figure 1. Edge-on photon absorption scheme.

2.3. Edge-on x-ray detector

In Arfelli *et al* (1997) and Rigon *et al* (2009), an edge-on structure was made with separated silicon strips, but that type of design is only applicable for x-rays with low energy (less than 35KeV) because of thickness limitation and area constraint for readout circuit. Since the current CCD technology provides a very high readout and post-processing rate, in this paper we propose a similar edge-on structure to obtain generated charges within different thicknesses and transfer the charges using the same charge transfer scheme as that for CCD.

As is shown in figure 1, the design resembles an ordinary metal-oxide-semiconductor (MOS) structure except that the bulk is far longer than the ordinary one because x-rays can travel a long distance inside silicon. In this design, the x-ray beam enters the silicon substrate from one side. As it travels inside the substrate, photons will interact with atoms and generate electrons. If a proper bias is applied on electrodes, generated charges will be collected in potential wells (PWs). Along the direction of the incident beam, the amount of charges in the first few PWs provides one constraint according to equation (4). Changing the numbers of PWs multiple times, we can obtain a number of equations corresponding to different thicknesses so that the energy distribution can be computed.

Before the collected charges can be quantified with an analog–digital converter (ADC), they need to be transferred from the substrate to the readout circuit. Here we adopt the same charge transfer approach as that for CCD. With proper biases applied on the electrodes, collected charges can be moved into its neighbor PW. A simple 3-phase charge transfer model is depicted in figure 2.

At time $t1$, only $v1$ is set to a high level so that generated charges can be collected in the potential well during exposure. At $t = t2$, both $v1$ and $v2$ are biased at a high level, without any barrier under the two gates the collected electrons can then flow to the PW under electrode $v2$. Finally, at $t = t3$, only $v2$ is biased at a high level, and all the electrons are transferred to the location under electrode $v2$. Similar procedures can be repeated over all the electrodes for collected charges to be transferred to the right most readout circuit.

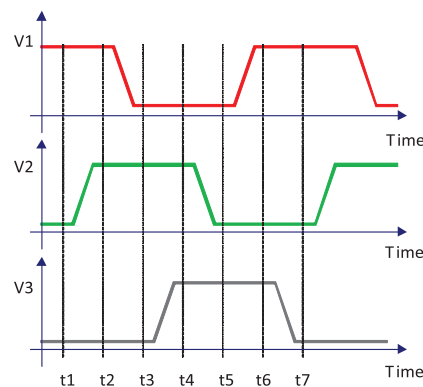


Figure 2. Pulse sequence for charge transfer.

3. Simulation results and analysis

In this study, we use the semiconductor device simulation tool Silvaco Atlas to evaluate the proposed structure. The simulation details are presented as follows:

(1) Physical models.

- a. For the carrier statistics model, we choose the Boltzmann model, which ignores carrier concentration reduction caused by heavy doping, since in our device, we do not have heavily doped regions.
- b. For the mobility model, the concentration dependent model is applied so that carrier mobility varies as concentration changes. Details are defined in look-up tables available for the simulating procedure. Parallel electric field dependence is also taken into account. As carriers are accelerated in an electric field their velocity will begin to saturate when the electric field magnitude becomes significant. These models are valid for normal temperatures (~ 300 K).
- c. For the recombination model, we adopt the Shockley–Read–Hall recombination, which considers the defects or traps within a forbidden band.

(2) Numerical methods.

There are many numerical methods available in the simulator such as Newton and Gummel. For our experiment, there is little difference between those methods. We used the Newton Iteration in our simulation where each iteration solves a linearized version of the nonlinear system.

The simulation procedure consists of three steps. First, we let 10 different monochromatic x-ray beams ranging from 10 keV to 100 keV act on the silicon bulk. Then, we increased the beam intensity from 1 W cm^{-2} to 10 W cm^{-2} step by step to obtain the corresponding charge responses. Finally, we used the composited x-ray beam of the same spectrum as real medical x-rays, and derived the energy distribution from charge information in PWs. For the real x-ray simulation, we took the GE_Maxiray_125 tube as the reference.

3.1. Device modeling

An overview of the 2D device model is in figure 3. The silicon substrate was $9,900 \mu\text{m}$ in length, which is sufficient to fully absorb photons under 20 keV, and absorbs a fraction of photons over 20 keV. The main parameters of this device are listed in table 1.

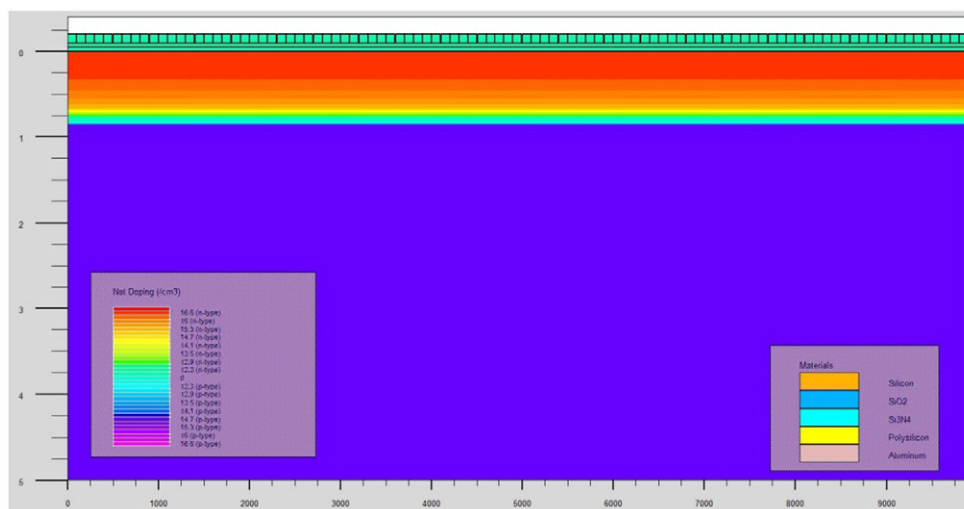


Figure 3. Device modeling with net doping.

Table 1. Device parameters.

Length	9900 μm (99 layers)
Width	5 μm
Electrode length	99 μm
P type doping	1×10^{15} per cm^3
N type channel	1×10^{10} per cm^3
Applied bias	−5 V to +5 V

When x-rays enter the depletion region, the width should be at least larger than the depletion region for a necessary bias to be applied to the gate. Hence, we used 5 μm as an example. Like in an ordinary CCD, we assumed the p^- type substrate in the simulation. Particularly, to minimize the dark current generated by surface traps or defects, we induced buried channel doping in the surface of the silicon bulk. Experiments have shown that the buried channel efficiently reduces the side effects caused by surface defects, meliorating charge transfer inefficiency (CTI) (Tompsett 1975, Hoople and Krusius 1991, Marcelot *et al* 2014). The device in the simulation tool is a mesh based structure, i.e., the whole device is divided into grids, which are simulation units. Limited by the computing capability, the number of grids should not be more than 20000. Some of the simulation parameters such as bulk length and width were constrained by the simulator. In practice, the device can be enlarged to handle higher energy x-rays and achieve higher resolving precision.

3.2. Photon absorption

When x-rays enter the device, electrons will be generated at different depths in the bulk. The fraction of photons being absorbed as a function of position is presented in figure 4. The photon absorption rate degrades as photon energy increases. As an x-ray beam can be regarded as a linear combination of radiations with different energies, responses of monochromatic radiations can then be substituted into equation (4) to obtain an approximate solution.

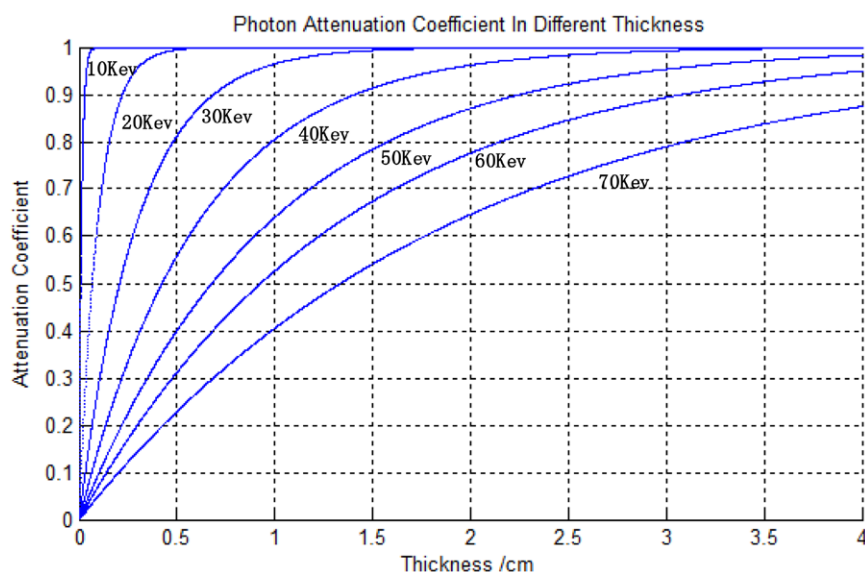


Figure 4. Photon attenuation as a function of position in the silicon bulk.

3.3. Photoelectric response

When a positive bias is applied to electrodes, a depletion region will form under the oxide layer. Generated electrons can then be collected in the depletion region driven by the electrical field, as shown in figure 1. During the collection process, a good device should have the following properties. The collection rate should be as fast as possible to meet high-speed CT needs, which is related to bias and doping concentration. During a limited time interval, charges collected in the PWs should be pure enough. Ideally, all the photon-generated electrons should be collected in PWs for analyzing and processing later, since detected photon electrons directly correspond to the incident beam spectrum. Clearly, not all charges collected in PWs are generated by photons, since a large fraction of electrons are thermions caused by doping and intrinsic carriers (known as the dark current).

It is possible to minimize the influence of the dark current. If radiation is removed while the bias is still on for the same time, then the collected electrons under this condition can be regarded as thermions, and we can obtain net photon-generated electrons by subtracting thermions from the total measurement. Figure 5 plots the charge responses to monochromatic x-rays from 10KeV to 100KeV as a function of beam intensity. The simulation results show that the generated charge density varies as the beam intensity increases with the relationship modeled in equation (5):

$$Pe = kI + d \quad (5)$$

where Pe is the collected electron density, k is determined by the x-ray energy, I is the beam intensity, and d is a constant related to the material. As no photoelectron is generated without radiation, d is generated by the dark current, being equal to $4e + 16$ per cm^3 in our simulation. Note that it requires different thicknesses to fully absorb x-rays of different energies, thus k varies as a function of photon energy and bulk thickness, which were obtained from the simulation. Actually, equation (5) is a special case of equation (4) as it takes monochromatic radiation that the coefficient k covers factors of attenuation, photon energy and photoelectron

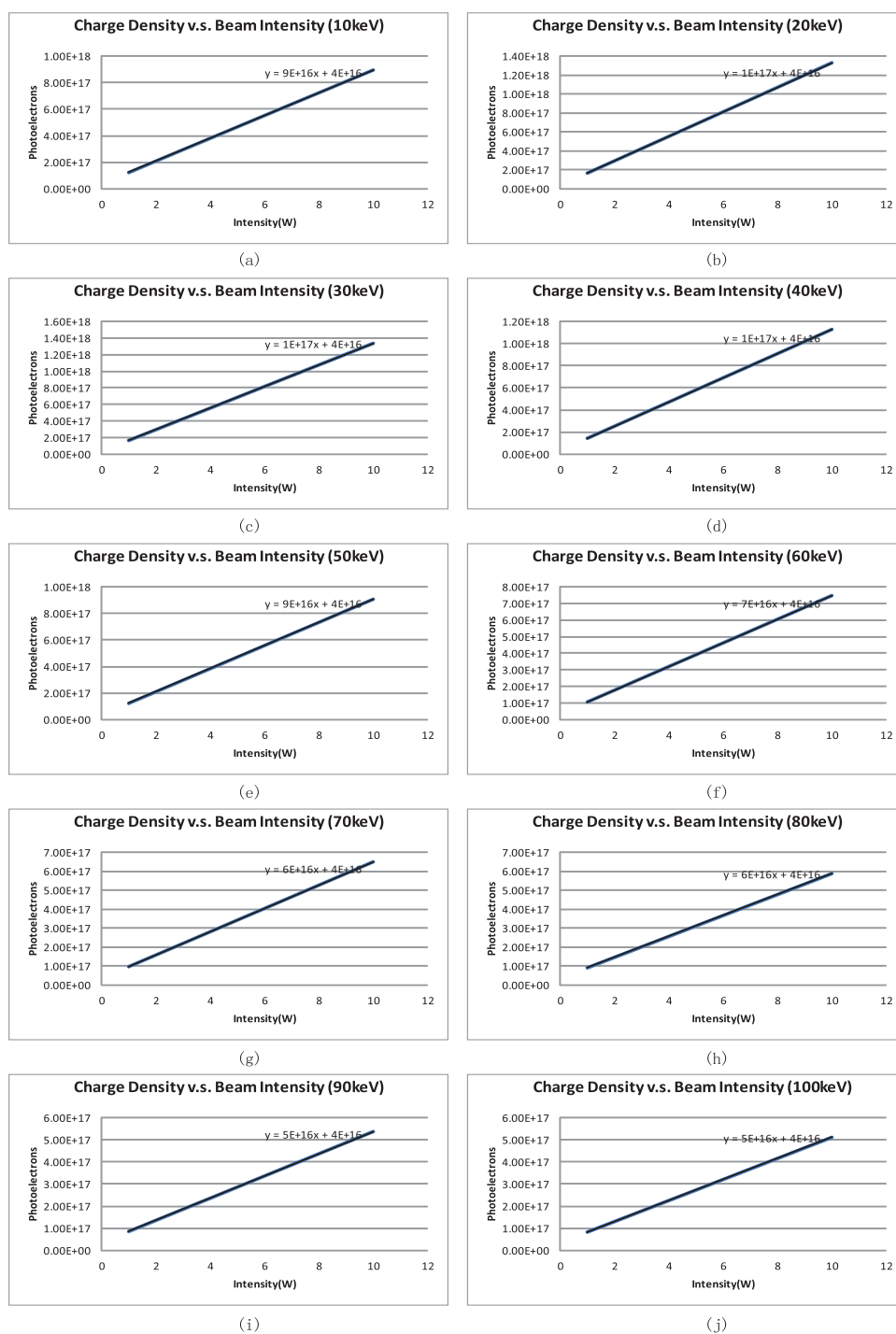
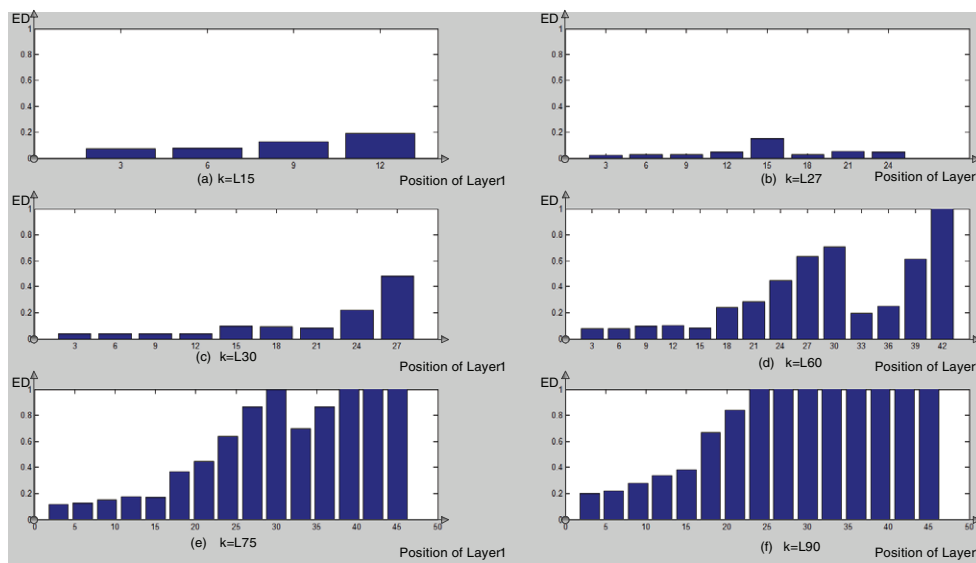


Figure 5. Generated photoelectrons versus beam intensity. (a)–(j) Charge responses to monochromatic radiation from 10 keV to 100 keV, respectively.

Table 2. Simulation results with exemplary composite radiations (ED: Euclidean distance).

Sim No.	Comp	Intensity	Layer	Separating position	Charge density	Resolved intensity	Error (in ED)
Exp1	10 keV	1w	1	L3	3.63×10^{17}	0.99w	0.05
	20 keV	2w	2	L27	6.59×10^{17}	2.02w	
	40 keV	4w	3	L99	1.27×10^{18}	3.95w	
Exp2	10 keV	1w	1	L3	3.24×10^{17}	1.01w	0.02
	20 keV	2w	2	L27	5.64×10^{17}	1.99w	
	60 keV	4w	3	L99	1.12×10^{18}	3.98w	
Exp3	15 keV	1w	1	L6	3.91×10^{17}	0.76w	0.30
	30 keV	2w	2	L72	9.25×10^{17}	1.89w	
	50 keV	4w	3	L99	1.19×10^{18}	4.15w	

**Figure 6.** Energy resolving errors. k denotes the separating position of the 2nd layer, the x -axis is the separating position of the 1st layer, and the y -axis is the error in the Euclidean distance.

generating rate. For further analysis, we assume that the substrate is horizontally uniform, which means that d is proportional to thickness.

Before dealing with real x-ray responses, a simple procedure for resolving the energy distribution is explained as follows. Let us assume three different composite beams, and each beam contains three different energy components, and then extract the charge information from the first three layers. In each case the extracted charge densities can be put into equation (6) to solve the energy distribution I :

$$\begin{bmatrix} k_{.11} & k_{.12} & k_{.13} \\ k_{.21} & k_{.22} & k_{.23} \\ k_{.31} & k_{.32} & k_{.33} \end{bmatrix} \begin{bmatrix} I_{.1} \\ I_{.2} \\ I_{.3} \end{bmatrix} + \begin{bmatrix} d_{.1} \\ d_{.2} \\ d_{.3} \end{bmatrix} = \begin{bmatrix} g_{.1} \\ g_{.2} \\ g_{.3} \end{bmatrix} \quad (6)$$

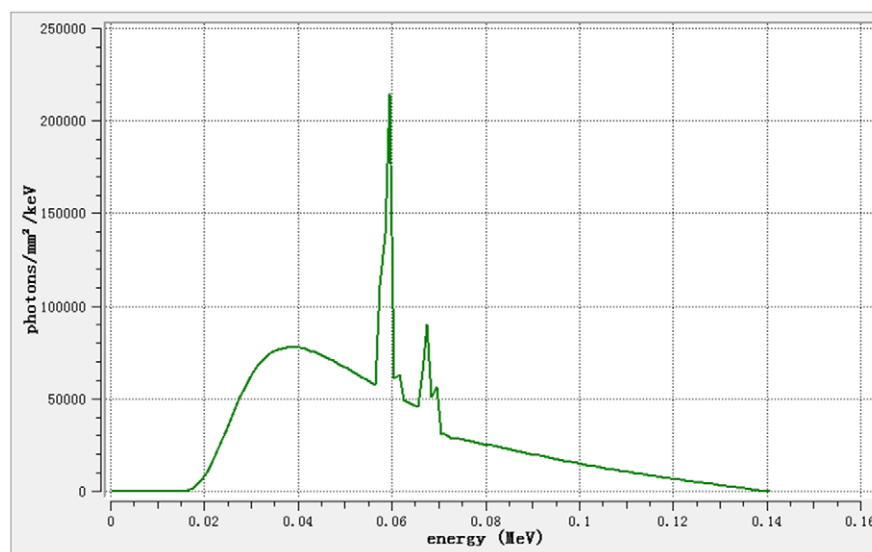


Figure 7. Energy spectrum of the GE_Maxiray_125 tube.

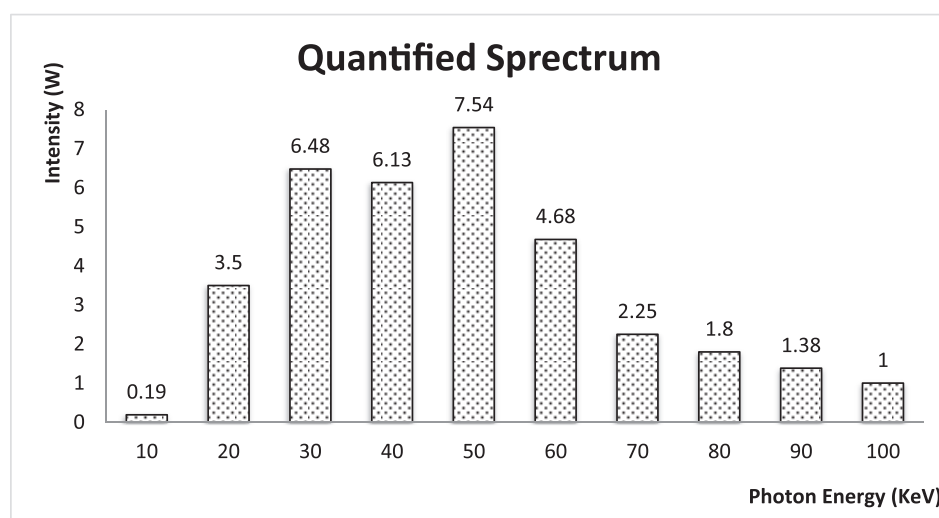


Figure 8. Discretized energy distribution as the reference.

The results are in table 2.

The layer thickness was not chosen arbitrarily, since we must ensure that equation (6) has a stable solution. For example, if layer 1 were long enough to fully absorb x-ray photons with energy 10 keV and 20 keV, then k_{i1s} and k_{i2s} would be almost identical, making the matrix \mathbf{K} singular. Note that experiment 3 yielded a greater error due to the limited bulk length that the best solution is beyond the structure in the simulation. In brief, the errors of the solved spectra seem acceptable in comparison with the original energy distribution, in support of our energy resolving approach.

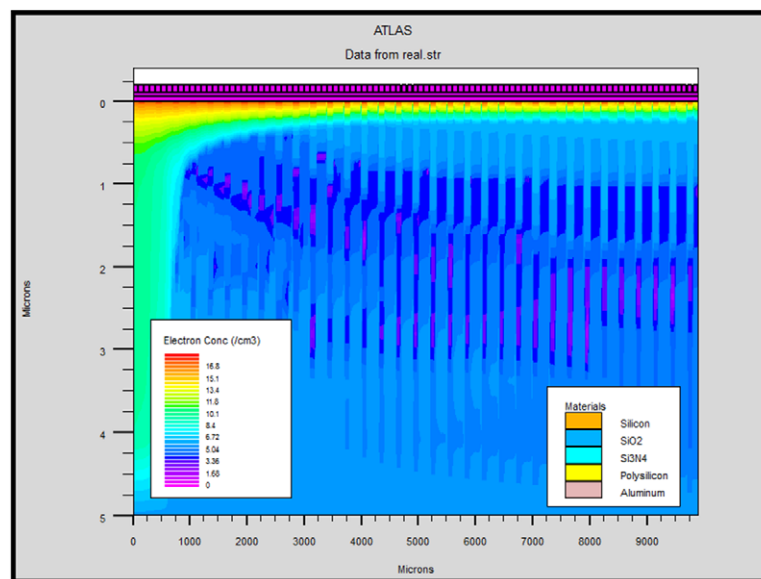


Figure 9. Photoelectric responses to the x-ray beam.

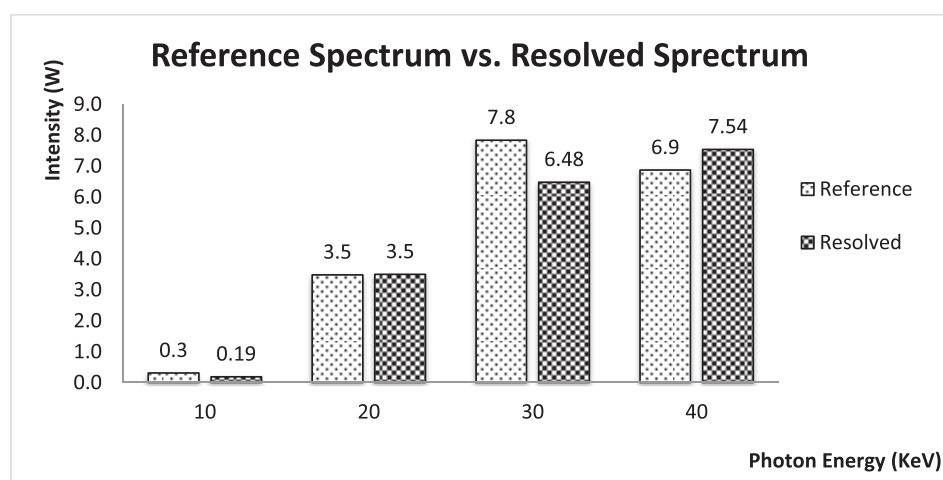


Figure 10. Resolved energy distribution in the four energy bins.

An exemplary optimizing procedure for Exp2 is presented as follows. The 3rd layer was fixed to L99. Then, we set six separating positions for the 2nd layer. For the six different positions, we adjusted the position of layer 1 and derived the corresponding energy distributions. Finally, we calculated the Euclidean distance between the resolved energy distribution and the original incident beam spectrum. The layer position corresponding to the minimum error is the optimized solution. Particularly, as seen in figure 6, the error of the resolved energy distribution varied little when the number of electrodes in the first layer was smaller than 20. To sum up, the optimization of separating points includes two steps; first the initial guess and then amendments based on dynamical grouping.

Table 3. Simulation results in eight energy bins.

Energy bins	5 keV	10 keV	15 keV	20 keV	25 keV	30 keV	35 keV	40 keV
Ref intensity (W)	0.1	0.2	1	2	3	3.3	3.6	4
Layer	1	2	3	4	5	6	7	8
Separating position	L3	L6	L9	L12	L27	L42	L66	L99
Charge density (/cm ³)	3.3×10^{17}	5.6×10^{17}	7.6×10^{17}	9.3×10^{17}	1.5×10^{18}	1.9×10^{18}	2.3×10^{18}	2.6×10^{18}
Resolved intensity (W)	0.099	0.19	1	1.99	3.02	3.15	3.97	3.78
Error (in ED)	0.4565							

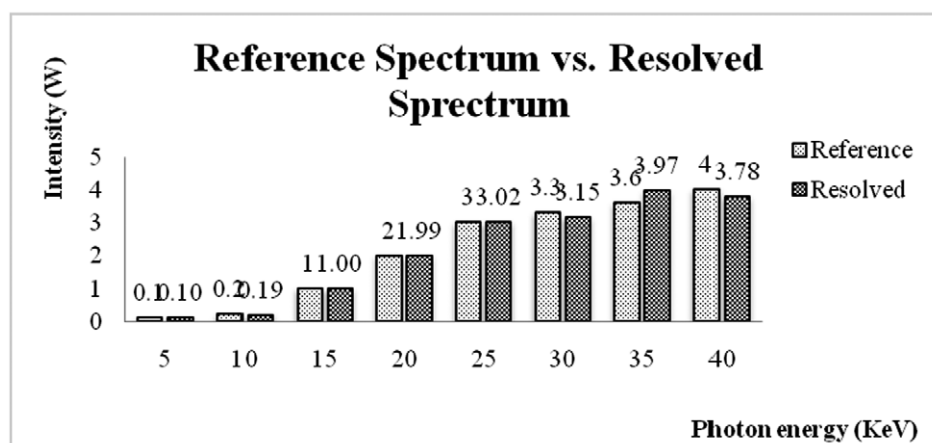


Figure 11. Results of eight energy bins under 40 keV.

To test the feasibility of our proposed energy-resolving approach, we further assumed the x-ray source with the same energy spectrum as that of the GE_Maxiray_125 tube. The spectrum is shown in figure 7.

In the simulation, the energy spectrum in figure 7 was quantified into 10 discrete energy bins from 10 keV to 100 keV. The quantified energy distribution is depicted in figure 8 as the true values.

Figure 9 gives the overview of a charged substrate in which photoelectrons were collected in PWs. Similar to subsection 3.1, the whole device had a length of 9900 μm and was separated into 10 equal layers. Although the layers were not optimized, we estimated four spectral components at discrete energies from the data collected in the 10 layers. As described above, we extracted data from the first 1, 2, 3, ..., 10 layers and put them into equation (6) to form a system of ten equations for a unique solution of the x-ray spectrum over the 10 energy bins. Since the substrate length limited accuracy over 40 keV, the distribution of high energies (>40 keV) was unreliable in this case. Resolved spectrum components of 10 keV, 20 keV, 30 keV and 40 keV are presented in figure 10.

To further evaluate our method, we considered more detailed x-ray responses under 40 keV. As shown in figure 11, we quantified the x-ray spectrum under 40 keV into 8 energy bins. Then, we repeated the procedure above, and obtained the resolved energy distributions with errors less than 0.46. This indicates that our approach is capable of deriving satisfactory results subject to the substrate length limitation. The results from this experiment are in table 3.

3.4. More realistic simulation

In our previous experiment, the number of energy bins resolved was the same as the number of input energy bins, which is not the case in real x-ray imaging studies. Medical x-rays have a continuous spectrum, which can be well approximated as a combination of many monochromatic components in narrow energy bins. Theoretically, we can accurately estimate the detected energy distribution when the number of input energy bins is the same as that of

unknown spectral components in all these energy bins. However, the estimation of spectral components in energy bins that are broader than those narrow bins are necessarily approximate. Nevertheless, this problem can be still solved as follows.

As an example shown in figure 12, the input x-rays consists of eight energy bins which are around 10 keV, 20 keV, ..., 70 keV and 80 keV, respectively, and we estimate spectral components in three broader energy bins around 10–30 keV, 40–50 keV and 70–80 keV, respectively. For energy-discriminative x-ray detection, we can place the electrodes to cover three intervals [0, 1], [1–2] and [2, 3] in units of cm, and form the corresponding equation (6). The coefficients in the system matrix K can be easily computed by assuming a known (such as uniform) energy distribution over each broad energy bin.

Another way is to induce a more specific rule that each separation point should be at the position so that x-ray energy in one input bin has been effectively absorbed. The following example illustrates this idea. In this case, incident x-rays have 40 energy bins ranging from 1 keV to 40 keV, and output energy bins are around 15 keV, 20 keV, 25 keV and 35 keV, respectively. Unmixing of these four energy bins consists of the following two steps.

Step 1: choose separation points. For the four energy bins to be resolved, three separation points are set at L27, L48 and L84 where photons with energy 15 keV, 20 keV and 25 keV are almost fully (>95%) absorbed at each point, respectively. Then, we have:

$$\begin{bmatrix} k_{11} & k_{12} & k_{13} & k_{14} \\ 0 & k_{22} & k_{23} & k_{24} \\ 0 & 0 & k_{33} & k_{34} \\ 0 & 0 & 0 & k_{44} \end{bmatrix} \begin{bmatrix} I_1 \\ I_2 \\ I_3 \\ I_4 \end{bmatrix} + \begin{bmatrix} d_1 \\ d_2 \\ d_3 \\ d_4 \end{bmatrix} = \begin{bmatrix} g_1 \\ g_2 \\ g_3 \\ g_4 \end{bmatrix} \quad (7)$$

Step 2: solve for spectral component from data in the output energy bins. Equation (7) can be solved recursively. To give a better understanding of the process, let us see the last line of equation (7).

$$k_{44} \times I_4 + d_4 = g_4 \quad (8)$$

As photons with energy lower than 25 keV are totally absorbed at L84, g_4 in equation (8) is basically generated by radiation in the range from 25 keV to 40 keV. Thus, I_4 in equation (8) is the spectral component in this energy interval. Similarly, I_1 , I_2 and I_3 correspond to the energy intervals 0–15 keV, 15–20 keV and 20–25 keV, respectively. To make the unmixing process more intuitive, we assumed that the x-ray intensity was the same in the narrow energy bins within each broad energy bin (Le and Molloy 2011). Figure 13 illustrates a typical unmixing outcome. The quality of energy resolving results depends on the required separation points which can be guaranteed if a sensor material is of a sufficient thickness.

3.5. Charge transfer

Charge transfer is the prerequisite for post-processing. The process of charge transfer between two adjacent electrodes is shown in figure 14, driven by the charge transfer logic explained in figure 2. In fact, transfer time is important in this scheme. A too short time cannot ensure that all the photon generated charges are transferred to the next electrode. Too long makes electrodes

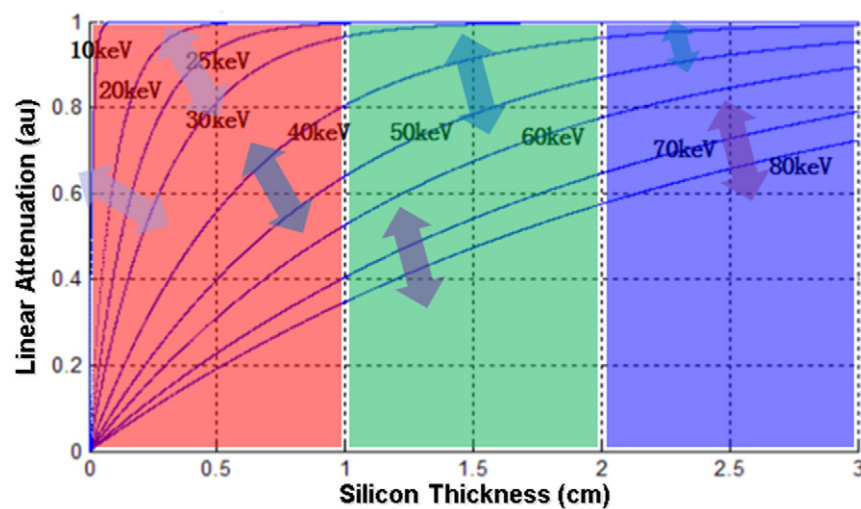


Figure 12. Information recovery in broad energy bins from projection data generated with a continuous x-ray spectrum.

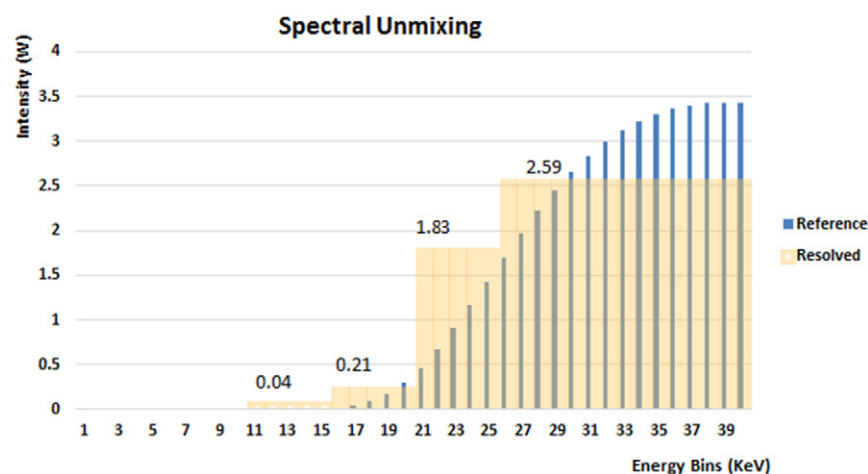


Figure 13. Estimated spectral components in 4 broad energy bins from data simulated in 40 input energy bins.

suffer more from the dark current. Our simulation shows that it took 1.05×10^{-7} s to transfer the collected charges to the next PW at a transfer efficiency of 0.999985. Under this condition, the maximum error in the transfer process would be rather small. In addition to the tradeoff of transfer time, surface defects also significantly affect the transfer efficiency. If a large amount of electrons are stuck in unpredictable surface traps, a substantial amount of charges will be lost in the transfer stage.

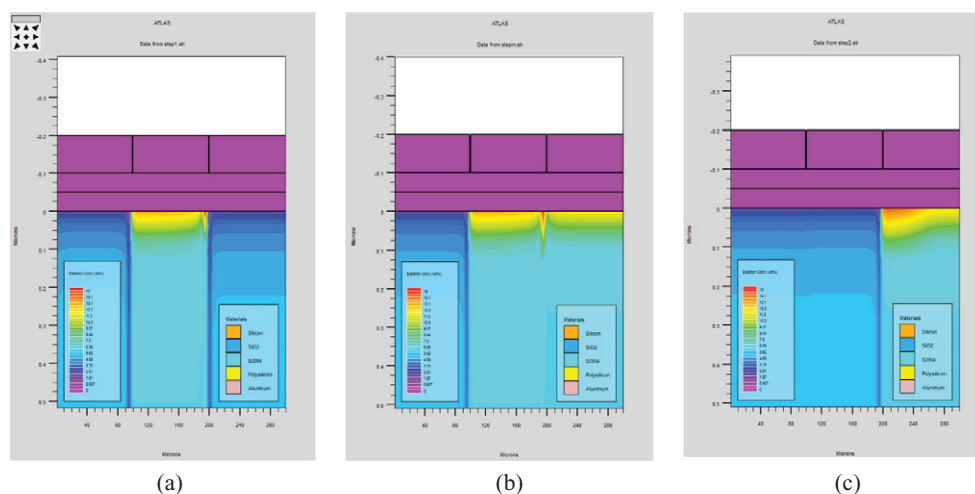


Figure 14. Charge transfer between adjacent electrodes. (a)–(c) Three steps presented in subsection 2.3.

4. Discussions and conclusion

The monochromatic response is the building block of our energy resolving scheme, which allows us to obtain k values (see equation (4)). For a desirable k , the device can be divided into k layers for k -independent measurements. The proposed energy-resolving approach can achieve a high precision if we optimally group electrodes to define the k layers and extract charge information.

A main error in estimating spectral signals comes from the layer separation, as is described in subsection 3.3. The length limitation is another factor, which could cause the result inaccurate. As seen in figure 4, the attenuation curves of photons over 60 keV are quite similar when the device length is smaller than 1 cm. Thus, the resultant equations would not be linearly independent. Furthermore, in section 3.3, we only estimated the x-ray spectrum in four energy bins. To resolve the measurement in more energy bins, errors must be minimized with respect to doping, dark current, layer thickness, and other factors.

In conclusion, the main contribution of this paper is the novel spectral sensing detector concept with the demonstrated feasibility of the silicon material. In the spirit of the CCD principle, we have shown the utility of the CCD-based charge transfer scheme in our detector architecture. In our design, the electrodes are dynamically grouped to collect energy sensitive data and compute spectrally specific line integrals. The two advantages of our proposed detector idea include (1) no counting-rate limitation and (2) cost-effectiveness from the mature technologies and widely-available material. To prototype such detectors, further efforts are needed, involving the design improvement, material optimization, and circuit development.

Acknowledgments

This paper was supported by the National High Technology Research and Development Program of China (863 program, No. 2012AA012705) and the National Natural Science Foundation of China (No. 61404090, No. 61306070). The authors gratefully acknowledge valuable comments by Qingzhen Meng and Jiaping Zhang with Tianjin University.

References

- Alvarez R E and Macovski A 1976 Energy-selective reconstructions in x-ray computerised tomography *Phys. Med. Biol.* **21** 733
- Arfelli F, Barbiellini G, Bonvicini V, Bravin A, Cantatore G, Castelli E, Di Michiel M, Longo R, Olivo A and Pani S 1997 An 'edge-on' silicon strip detector for x-ray imaging *IEEE Trans. Nucl. Sci.* **44** 874–80
- Bertolini G and Coche A 1968 *Semiconductor Detectors* (New York: Wiley) ch 5
- Bornefalk H and Danielsson M 2010 Photon-counting spectral computed tomography using silicon strip detectors: a feasibility study *Phys. Med. Biol.* **55** 1999
- Burke B, Mountain R, Daniels P, Cooper M and Dolat V 1994 CCD soft x-ray imaging spectrometer for the ASCA satellite *IEEE Trans. Nucl. Sci.* **41** 375–85
- Chu J, Cong W, Li L and Wang G 2013 Combination of current-integrating/photon-counting detector modules for spectral CT *Phys. Med. Biol.* **58** 7009
- Doran S J, Koerkamp K K, Bero M A, Jenneson P, Morton E J and Gilboy W B 2001 A CCD-based optical CT scanner for high-resolution 3D imaging of radiation dose distributions: equipment specifications, optical simulations and preliminary results *Phys. Med. Biol.* **46** 3191
- Giersch J, Niederlöhner D and Anton G 2004 The influence of energy weighting on x-ray imaging quality *Nucl. Instrum. Methods Phys. Res. A* **531** 68–74
- Gruner S M, Tate M W and Eikenberry E F 2002 Charge-coupled device area x-ray detectors *Rev. Sci. Instrum.* **73** 2815–42
- Hoople C R and Krusius J P 1991 Characteristics of submicrometer gaps in buried-channel CCD structures *IEEE Trans. Electron Devices* **38** 1175–81
- Le H Q and Molloy S 2011 Segmentation and quantification of materials with energy discriminating computed tomography: a phantom study *Med. Phys.* **38** 228–37
- Lundqvist M, Cederstrom B, Chmili V, Danielsson M and Nygren D 1999 Computer simulations and performance measurements on a silicon strip detector for edge-on imaging *IEEE Nuclear Science Conf. Record.* 1 pp 433–8
- Marcelot O, Estribeau M, Goiffon V, Martin-Gonthier P, Corbiere F, Molina R, Rolando S and Magnan P 2014 Study of CCD transport on CMOS imaging technology: comparison between SCCD and BCCD, and ramp effect on the CTI *IEEE Trans. Electron Devices* **61** 844–9
- Overdick M, Bäumer C, Engel K J, Fink J, Herrmann C, Krüger H, Simon M, Steadman R and Zeitler G 2009 Status of direct conversion detectors for medical imaging with x-rays *IEEE Trans. Nucl. Sci.* **56** 1800–9
- Pan D, Roessl E, Schlomka J P, Caruthers S D, Senpan A, Scott M J, Allen J S, Zhang H, Hu G and Gaffney P J 2010 Computed tomography in color: nanoK-enhanced spectral CT molecular imaging *Angew. Chem.* **122** 9829–33
- Persson M, Huber B, Karlsson S, Liu X, Chen H, Xu C, Yveborg M, Bornefalk H and Danielsson M 2014 Energy-resolved CT imaging with a photon-counting silicon-strip detector *Phys. Med. Biol.* **59** 6709
- Rigon L, Arfelli F, Astolfo A, Bergamaschi A, Dreossi D, Longo R, Menk R-H, Schmitt B, Vallazza E and Castelli E 2009 A single-photon counting 'edge-on' silicon detector for synchrotron radiation mammography *Nucl. Instrum. Methods Phys. Res. A* **608** S62–5
- Shikhaliev P M 2008 Energy-resolved computed tomography: first experimental results *Phys. Med. Biol.* **53** 5595
- Shikhaliev P M 2009 Projection x-ray imaging with photon energy weighting: experimental evaluation with a prototype detector *Phys. Med. Biol.* **54** 4971
- Taguchi K, Frey E C, Wang X, Iwanczyk J S and Barber W C 2010 An analytical model of the effects of pulse pileup on the energy spectrum recorded by energy resolved photon counting x-ray detectors *Med. Phys.* **37** 3957–69
- Taguchi K and Iwanczyk J S 2013 Vision 20/20: single photon counting x-ray detectors in medical imaging *Med. Phys.* **40** 100901
- Tompsett M F 1975 Surface potential equilibration method of setting charge in charge-coupled devices *IEEE Trans. Electron Devices* **22** 305–9